Supplementary Information

Competitive solvent occupation chemistry enabling robust four-electron conversion for anti-freezing aqueous zinc-iodine batteries

Wenyu Xu[1], Zelin Chang[1], Hongwei Wang[1], Binfen Wang[1], Hongbo Ding[1], Jijian Xu[2]*, Xinliang Li[1]*

[1]School of Physics and Laboratory of Zhongyuan Light, Zhengzhou University, Zhengzhou 450052, China

[2]Department of Chemistry, City University of Hong Kong, Hong Kong, 999077, China

E-mail: lixinliang@zzu.edu.cn; jijianxu@cityu.edu.hk

Methods

Materials

All chemicals were used as received directly without any further treatment. Zinc sulfate heptahydrate ($ZnSO_4 \cdot 7H_2O$, 99%, Aladdin), zinc perchlorate hexahydrate ($Zn(ClO_4)_2 \cdot 6H_2O$, anhydrous, 99.95% metal basis, ALFA), ammonium chloride (NH_4Cl, 99%, Aladdin), polyethylene glycol (PEG, Aladdin), lithium chloride (LiCl, 99%, Aladdin), potassium chloride (KCl, 99%, Aladdin), sodium chloride (NaCl, 99%, Aladdin). Activated Carbon (YP-50, Kurraray, Japan), and carbon cloth (CC, W0S1011) were purchased from Suzhou Sinero Technology Co., Ltd. Zn foil (99.9%, 100 μm, Canrd), N-methyl-2-pyrrolidone (NMP, 99%, Aladdin), poly(vinylidene fluoride) (PVDF, average Mw ~ 400,000, Aladdin).

Preparation of cathode electrode and electrolyte

Carbon cathodes were prepared by mixing YP50, acetylene black, and PVDF at a mass ratio of 7:2:1 in NMP for 4 hours. The uniform mixture was coated onto carbon cloth current collectors, then vacuum dried at 80 °C for 24 hours. The areal loading reached 2 mg cm^{-2}. Circular electrodes with a diameter of 12 mm were punched and reserved. SnI_4 was dissolved uniformly in ethanol to obtain a stable suspension. A total of 32 μL of the suspension was deposited onto the carbon cathode discs in multiple aliquots with uniform coverage, then dried at ambient temperature for 48 hours, yielding SnI_4 cathodes.

Polyethylene glycol (PEG, weight-average molecular weight Mw = 400 kg mol^{-1}) was used as the co-solvent. All electrolytes were formulated with 0.5 mol kg^{-1} $Zn(ClO_4)_2$ and 0.5 mol kg^{-1} NH_4Cl, with the PEG mass fraction in the total solvent adjusted to 0 *wt.%*, 50 *wt.%*, 70 *wt.%* and 90 *wt.%*, denoted as CN0, CN5, CN7 and CN9, respectively. For chloride salt control groups, electrolytes were prepared with 70 *wt.%* PEG, with only the chloride salt species changed while all solute concentrations and solvent compositions remained unchanged.

Characterizations

UV-*vis* spectra were measured on a Shimadzu UV-3600 Plus Ultraviolet instrument. *In-situ* Raman spectra were captured by the Horiba LabRam HR Evolution equipped with a 532 nm laser and a special battery testing device. Grazing-incidence X-ray diffraction (GIXRD) analysis was performed on Empyrean (PANalytical) with Cu Ka radiation (λ = 1.54056 Å). Differential scanning calorimetry-thermogravimetric (DSC-TGA) were conducted by NETZSCH 3500. In the *in-situ* non-invasive dark-field light imaging (DFLI) test, the excess electrolyte and charge/discharge time were used to promote massive microdroplet generation, making the effect more pronounced. X-ray absorption fine structure (XAFS) spectroscopy was carried out using the Rapid XAFS 2M (Anhui Absorption Spectroscopy Analysis Instrument Co., Ltd.) by transmission mode at 20 kV and 40 mA. Time of flight secondary ion mass spectrometry (TOF-SIMS) measurements were conducted on an ION-TOF GmbH TOF SIMS 5 instrument.

Electrochemical measurements

For static full batteries, the CR2032 coin-type batteries were assembled for the electrochemical properties test. For a symmetric Zn||Zn battery, Zn foils were used as both cathode and anode. Cyclic voltammetry (CV) and electrochemical impedance spectroscopy (EIS) data were acquired using a CHI760E electrochemical workstation. Galvanostatic charge-discharge (GCD) testing, rate capability, and galvanostatic intermittent titration technique (GITT) analyses were performed using LAND CT2001A battery testing equipment.

Calculation method

MD simulations were carried out using the LAMMPS package. The OPLS-AA force field with fitted parameters for ClO_4^- anions, NH_4^+ cations, and PEG molecules (from LigParGen) was used in this work. Water molecules were simulated with the TIP3P-FB model, and the parameters of the Zn^{2+} and Cl^- were adopted from Merz Jr's results.

Parameter fitting was performed using the density functional theory (DFT) package Gaussian16 under B3LYP exchange-correlation functional with Grimme's DFT-D3(BJ) empirical dispersion correction, and the def2-TZVP (for neutral molecules) and the ma-TZVP (for anions) basis set was adopted for self-consistent field (SCF) calculations.

The RESP2(0.5) charges combining gas- and liquid-phase (implicit solvent, PCM model) charges were adopted for ClO_4^- anions, NH_4^+ cations, and PEG molecules in this work, calculated using Gaussian16 and the Multiwfn package.

The pure water system contains 3889 H_2O molecules, 70 $Zn(ClO_4)_2$, and 35 NH_4Cl; the PEG-H_2O system contains 1167 H_2O molecules, 119 PEG molecules,70 $Zn(ClO_4)_2$, and 35 NH_4Cl. The systems were initialized using the Packmol package and the Moltemplate package. The systems were then subjected to a simulated annealing equilibration protocol as follows: (1) equilibration at T = 298 K for 2 ns in NPT ensemble; (2) heating up the system to 500 K over 2 ns in NPT ensemble; (3) relaxation at T = 500 K over 2 ns in NPT ensemble; (4) cooling down to T = 298 K over 2 ns in NPT ensemble; (5) equilibration at T = 298 K for 50 ns in NPT ensemble. The production run was subsequently performed at the specified temperature over 50 ns in the NVT ensemble. All the simulations in this work used a timestep of 2 fs and a pressure of 1 atm. The temperature and pressure were regulated with a Nose-Hoover thermostat and barostat, with a damping parameter of 0.2 ps and 2 ps, respectively.

All the calculations involving binding energy in this article were performed with Gaussian16. Optimization was finished at B3LYP/def2-SVP level with Grimme's DFT-D3 empirical dispersion correction. Single point energy was calculated at M06-2X/ma-TZVP level. The PCM implicit solvent model was applied.

Supplementary Note 1. Calculation of Cl^- diffusion coefficient (D_{Cl^-}) based on electrochemical impedance spectroscopy (EIS)

The ion diffusion coefficients were calculated from EIS spectra according to the following equation:

$$D_{Cl} = 0.5\left[\frac{RT}{n^2F^2AC\sigma}\right]^2$$

Where R is the gas constant (8.314 J K^{-1} mol^{-1}), T is the room temperature (298.15 K), A is the surface area of the electrode (1.13 cm^2), n is the number of electrons transferred (1), F is the Faraday constant (96500 C mol^{-1}), C is the concentration of Cl^- (0.5×10^{-3} mol cm^{-3}), and σ is the slope of the plot of Z, against $\omega^{-1/2}$ based on $Z' = R_s + R_{ct} + \sigma\omega^{-1/2}$.[1]

Supplementary Note 2. Calculation of *b* value

In principle, the relative contributions of the surface-controlled effect (k_1v) and diffusion processes ($k_2v^{1/2}$) could be quantitatively determined by the following equation:

$$i = k_1v + k_2v^{1/2}$$

Where k_1 and k_2 are the corresponding constants at different sweep rates.[2-4]

Supplementary Note 3. Calculation of Cl^- diffusion coefficient (D_{Cl}) based on galvanostatic intermittent titration technique (GITT)

Ionic diffusivity was determined using the GITT. The total ionic diffusion coefficient (D_{Cl}) is calculated by the following equation:

$$D_{Cl} = \frac{4}{\pi\tau}\left(\frac{n_mV_m}{S}\right)^2\left(\frac{\Delta E_S}{\Delta E_t}\right)^2$$

Where τ is the duration of the current pulse, n_m, and Vm are the mole number (mol) and molar volume (cm^3 mol^{-1}); S is the total contacting area between electrode and electrolyte; ΔE_S is the voltage change between two adjacent equilibrium states; and ΔE_t is the voltage change induced by the galvanostatic charge-discharge.[5, 6]

Supplementary Note 4. DRT

In-situ EIS measurements were conducted in parallel using a CHI700E electrochemical workstation under galvanostatic cycling at 0.1 A g^{-1}, with EIS spectra

acquired at 0.2 V potential intervals (frequency range: 0.1-10^5 Hz) and subsequently analyzed via DRT tools software (a MATLAB-based specialized EIS analysis tool) to derive the distribution of relaxation time (DRT) curves. The impedance spectra were transformed using the $\gamma(\ln\tau)$ relaxation function model (where characteristic peak positions correspond to specific relaxation times $\tau = 1/f$), enabling the identification of distinct electrochemical processes through peak localization and impedance quantification via peak area analysis.[7, 8]

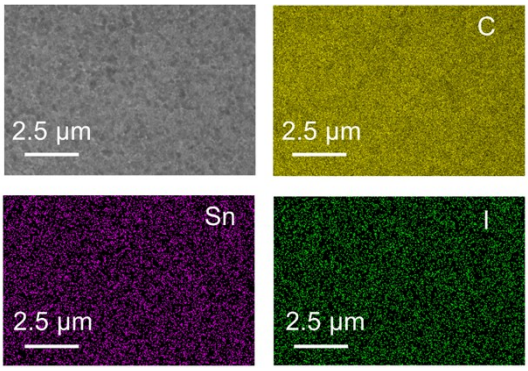

Fig. S1. SEM and EDS mapping images of the SnI_4 cathode.

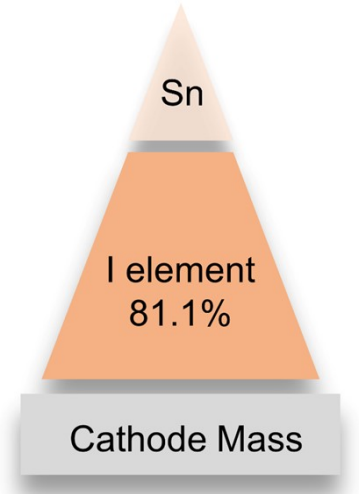

Fig. S2. The ratio of active materials in the SnI_4 cathode.

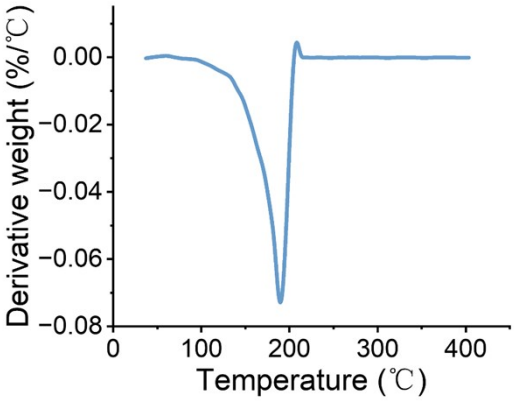

Fig. S3. DSC curve of SnI_4.

Fig. S4. The color of the deionized water solution over time after adding SnI_4.

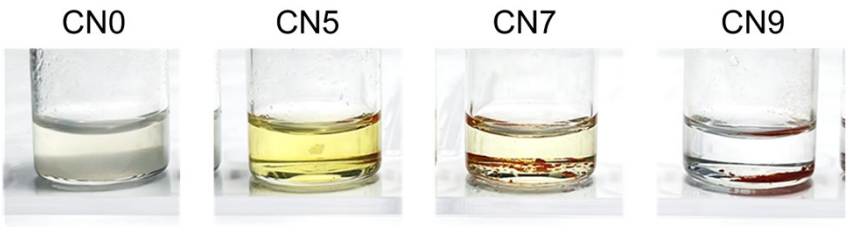

Fig. S5. The color of CN0, CN5, CN7, and CN9 electrolytes over time after adding SnI_4.

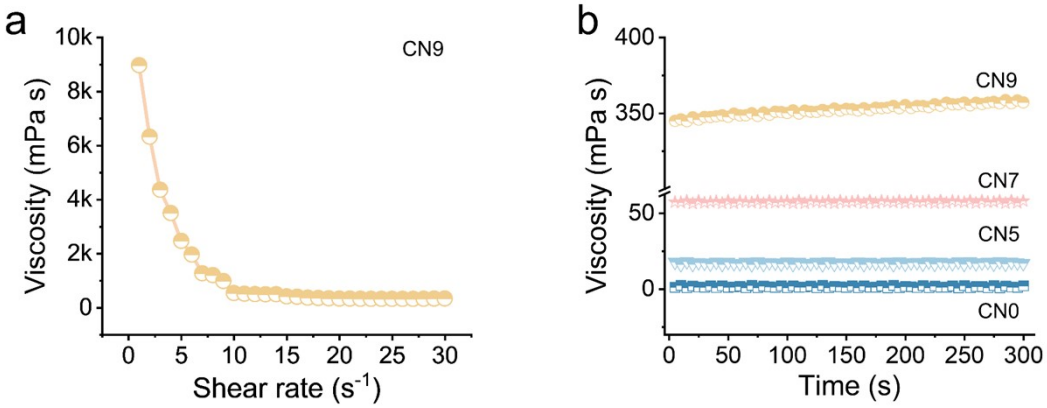

Fig. S6. (a) Determination of the shear rate range based on steady-state results from pre-tests of the CN9 electrolyte. (b) Viscosity *vs.* time curves of CN7 and CN9 electrolytes at a shear rate of 25 s^{-1}.

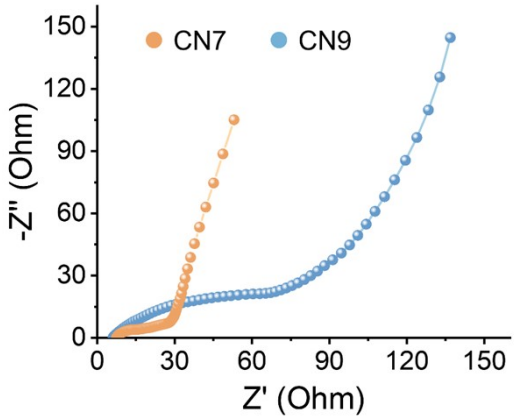

Fig. S7. The EIS spectra of CN7 and CN9 electrolytes.

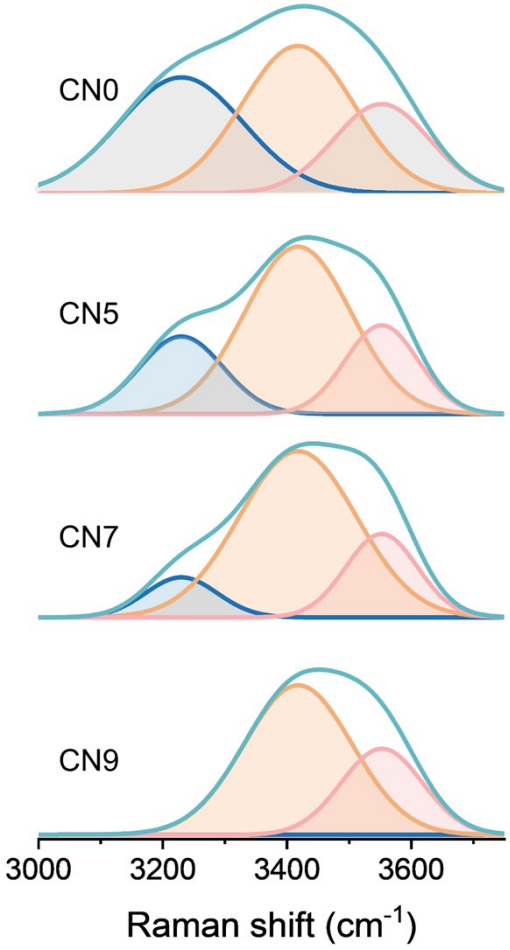

Fig. S8. The Raman spectra of O-H stretching.

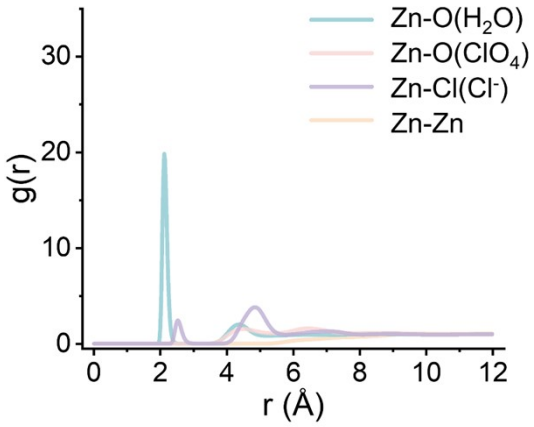

Fig. S9. RDFs of Zn-O in CN0 electrolyte.

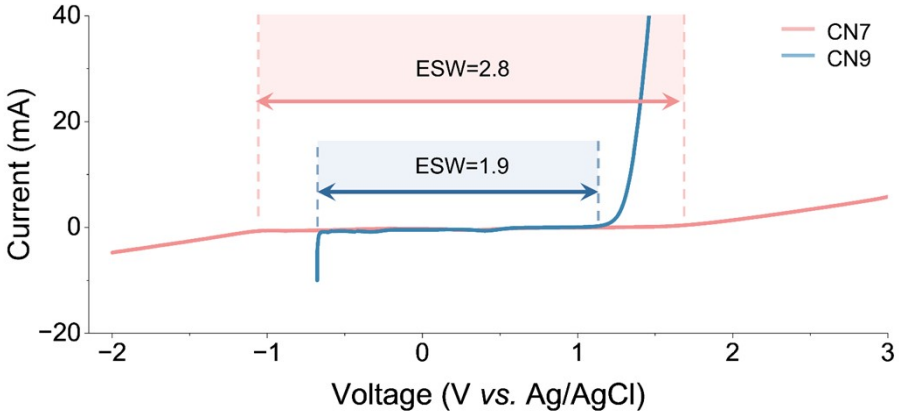

Fig. S10. LSV curevs of CN0 and CN7 electrolytes in three-electrode sysytem.

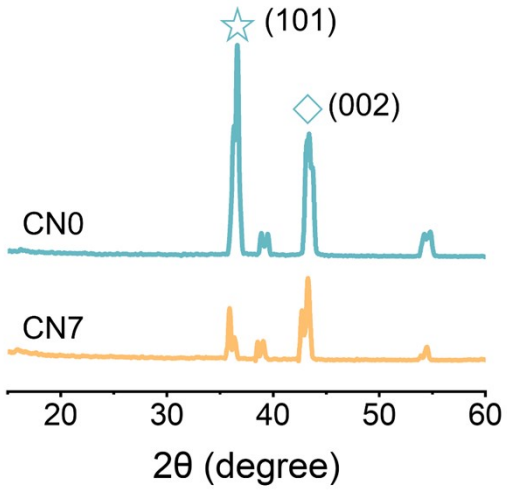

Fig. S11. GIXRD patterns of Zn foil after cycling in CN0 and CN7 electrolytes at 0.5 mA cm^{-2}/0.5 mAh cm^{-2}.

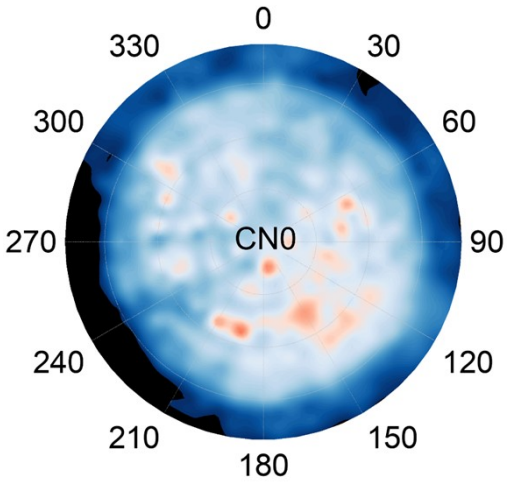

Fig. S12. (002) pole figure of Zn anode in CN0 electrolyte after 100 cycles of 0.5 mA cm^{-2}/0.5 mAh cm^{-2}.

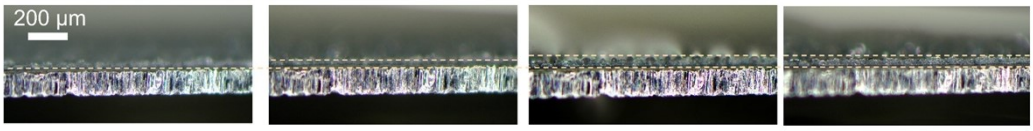

Fig. S13. *In-situ* optical microscopy images of the Zn plating process in CN7 electrolyte.

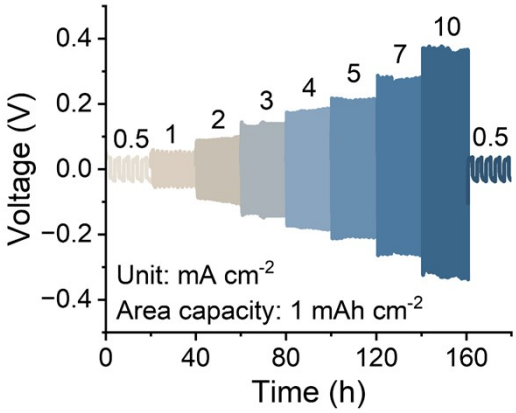

Fig. S14. Rate performance of Zn||Zn battery with CN7 electrolyte from 0.5 to 10.0 mA cm^{-2}.

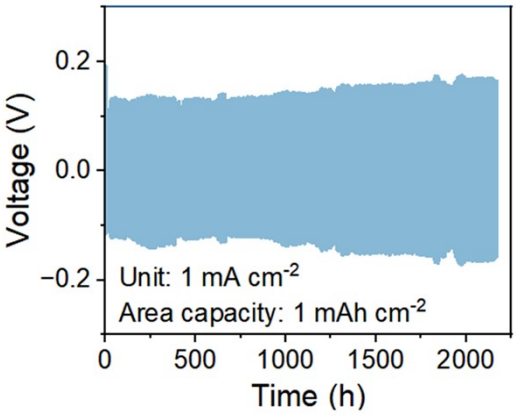

Fig. S15. Voltage profiles of Zn||Zn battery with CN7 electrolyte at 1.0 mA cm^{-2}/1.0 mAh cm^{-2}.

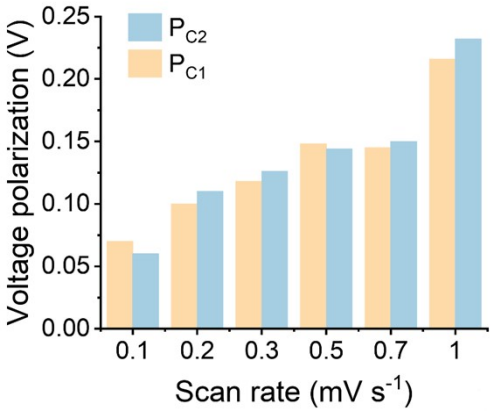

Fig. S16. The voltage polarization of peak R_1 and R_2 of CV curves in the range of 0.1-1 mV s^{-1}.

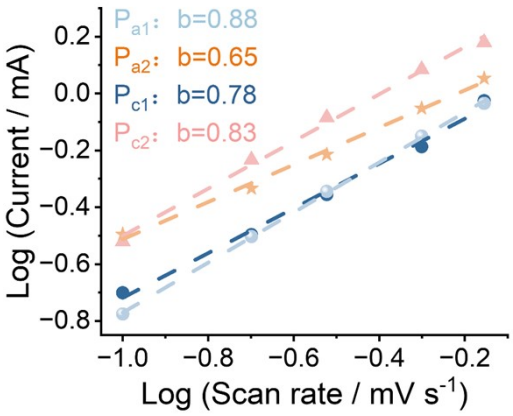

Fig. S17. Relationship between peak current and the square root of scanning rate ranging from 0.1-5.0 mV s^{-1}.

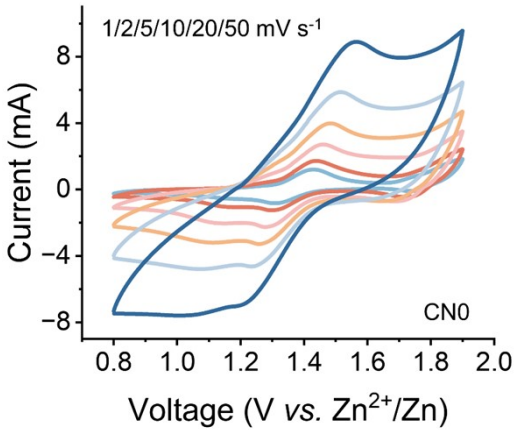

Fig. S18. CV curves of Zn||SnI_4 battery in CN0 electrolyte within 1.0 – 50.0 mV s^{-1}.

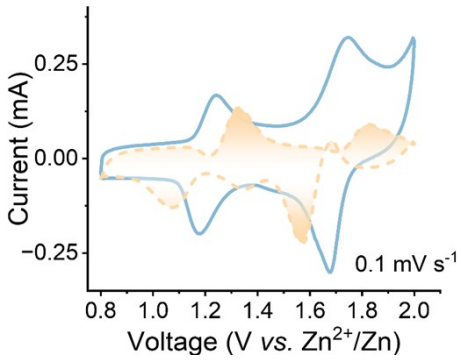

Fig. S19. Illustration of capacitive contribution at 0.1 mV s^{-1}.

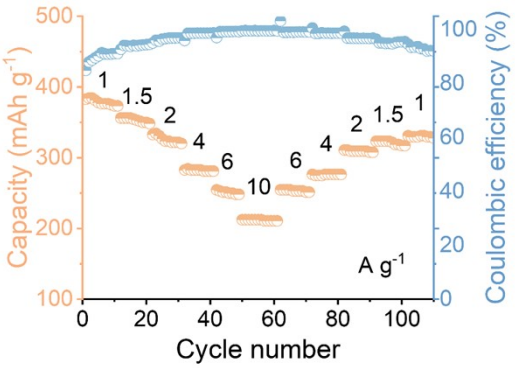

Fig. S20. Rate performance of the battery at a wide range of current densities, ranging from 1.0 to 10.0 A g^{-1}.

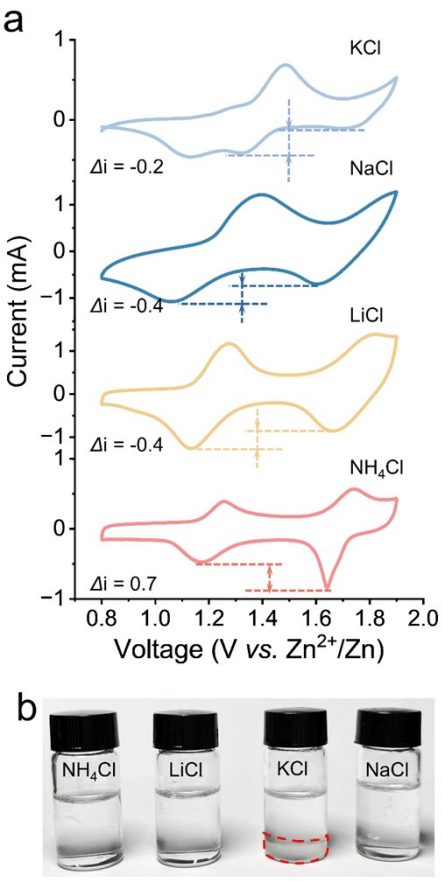

Fig. S21. (a) CV curves of of Zn||SnI_4 battery in LiCl, KCl, NaCl-based electrolytes at 1.0 mV s^{-1}. **(b)** Optical photographs of different chloride salts in 70 *wt.*% PEG + 1 m $Zn(ClO_4)_2$, with incomplete dissolution and bottom precipitation of KCl-based electrolyte observed after 24 h of standing.

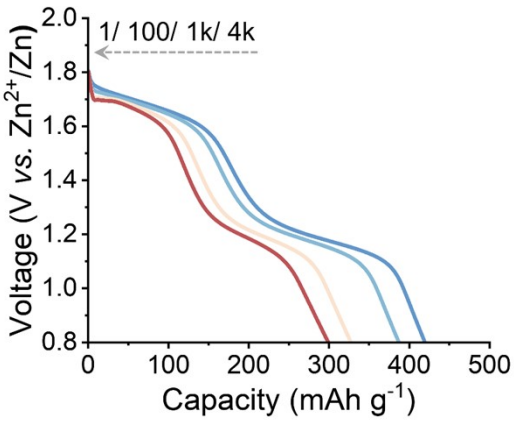

Fig. S22. GCD curves of the 1st, 100th, 1000th, and 4000th cycle of the battery at 2.0 A g^{-1}.

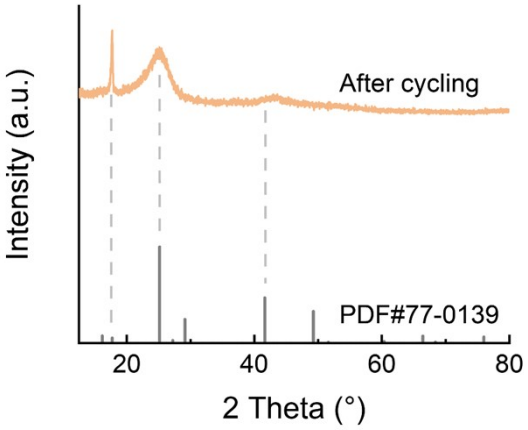

Fig. S23. Powder diffraction file card of SnI_4 and XRD patterns of SnI_4 cathode after 200 cycles at 1.0 A g^{-1}.

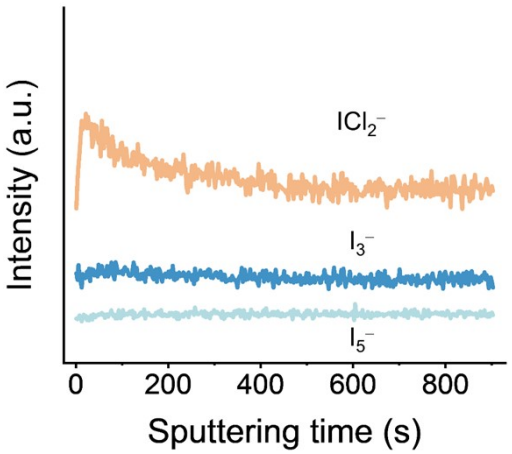

Fig. S24. TOF-SIMS negative in-depth ion profiles.

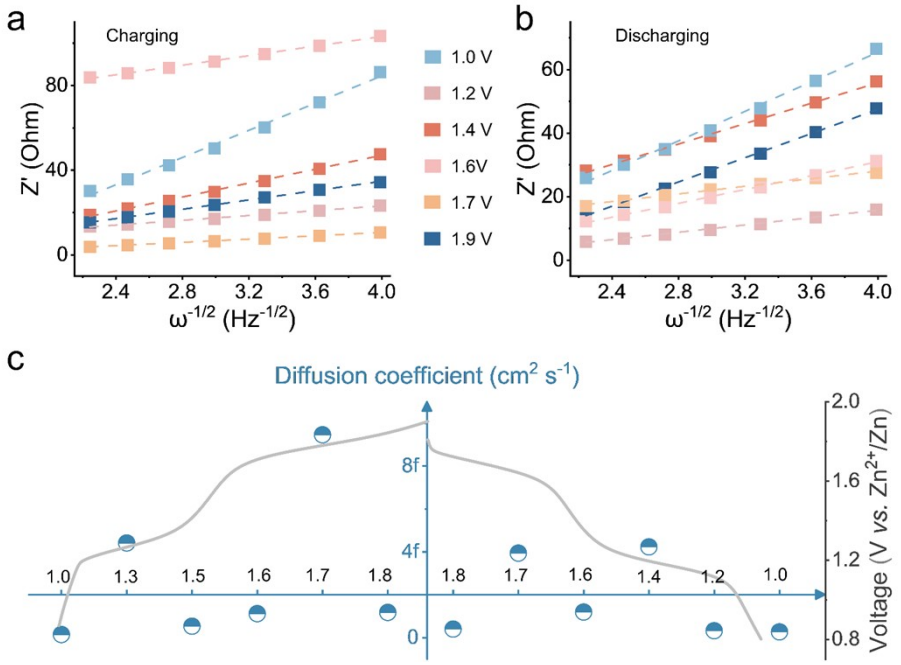

Fig. S25. (a) Corresponding plots of *Z'* against $\omega^{-1/2}$ during charging process. **(b)** Corresponding plots of *Z'* against $\omega^{-1/2}$ during discharging process. **(c)** Fitted ion diffusion coefficients (D_I) derived from *ex-situ* EIS measurements.

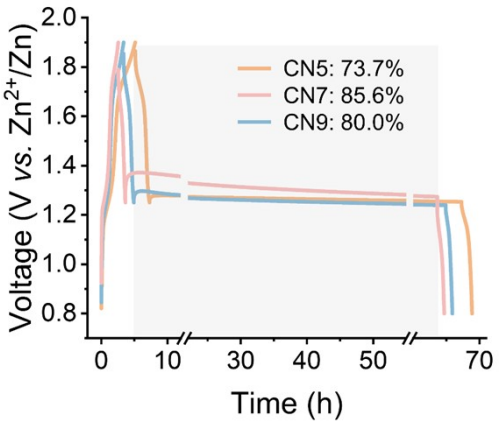

Fig. S26. Voltage profiles with 48 hours rest in fully discharged state with different electrolytes.

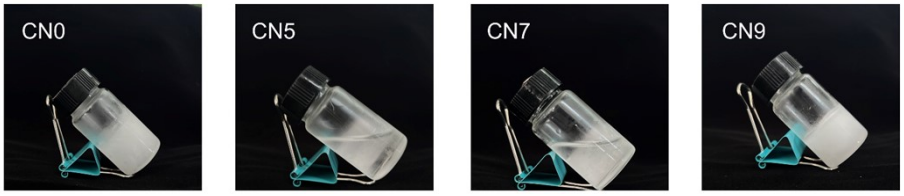

Fig. S27. Optical images of CN0, CN5, CN7, and CN9 electrolytes at -20 °C.

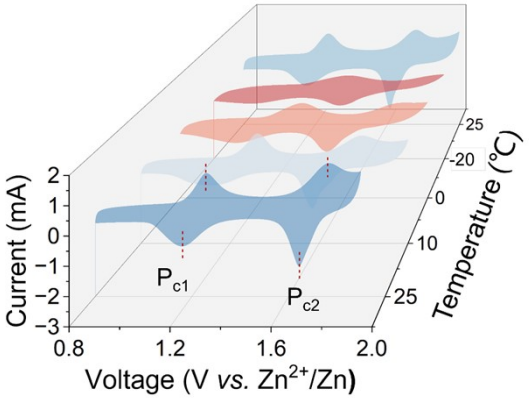

Fig. S28. CV curves of Zn||SnI_4 battery at different temperatures from 25 °C to -20 °C at 1 mV s^{-1}.

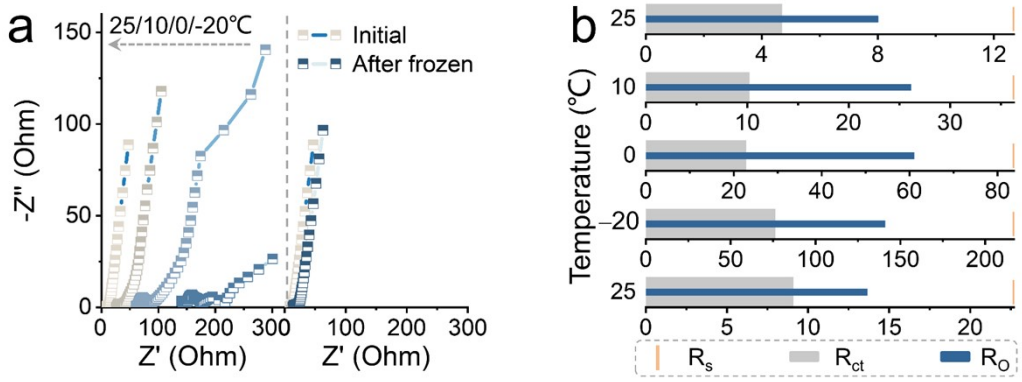

Fig. S29. (a) EIS spectra of Zn||SnI_4 battery at different temperatures from 25 °C to -20 °C. **(b)** Temperature-dependent internal resistance derived from EIS.

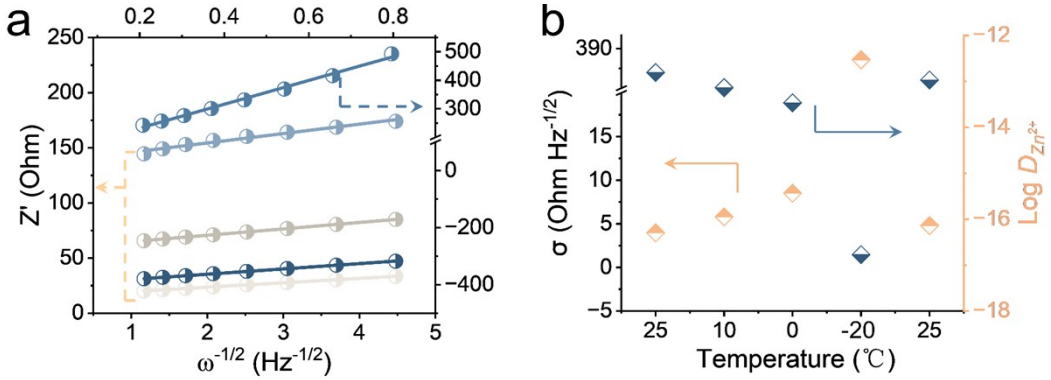

Fig. S30. (a) Corresponding plots of Z' against $\omega^{-1/2}$. **(b)** Fitted ion diffusion coefficients (D_I).

Table. S1. Comparison of various performance parameters with those reported for AZIBs cathodes.

Cathode	Total capacity ($mAh\ g^{-1}$)	Contribution of $I^{0/+}$ (%)	Mass ratio of cathode (%)	Ref.
I_2@AC	560.4	35.7	34.3	9
I_2@AC	412.0	48.5	20.0	10
I_2@AC	355.5	42.2	20.0	11
Ni-Fe-I-LDH	350.0	37.1	10.0	12
I_2@NBOC	414.5	38.6	24.0	13
I_2@AC	389.4	38.9	30.7	14
PVPI	419.0	35.8	34.8	15
BPD-HI	385.0	39.0	43.2	16
I_2@KB	418.9	49.8	40.0	17
I_2@KB	317.5	39.4	40.0	18
I_2@AC	350.0	42.9	40.0	19
FeSA-I_2	524.0	43.2	26.6	20
PAC@I_2	589.0	42.4	20.0	21
I_2@AC	450.0	44.4	28.0	22
$Ti_3C_2I_2$	207.0	45.4	20.0	23
BiI_3	270.0	37.0	38.8	24
SnI_4	375.0	73.0	73.0	This work

Supplementary Table 2. Detailed data on the capacity contribution from the I^0/I^+ conversion reaction at different current densities, based on the four-electron conversion mechanism.

Concentration of Cl^- in electrolyte (M or m)	Current density ($A\ g^{-1}$)	Capacity above 1.25 V ($mAh\ g^{-1}$)	Contribution of I^0/I^+ (%)	Ref.
	1	109.07	45.9	11
2 M $ZnSO_4$ + 0.5	2	70.93	45.8	
M NaCl	5	91.46	39.4	
	8	73.03	33.9	
	1	194.16	49.6	25
3 m $Zn(OTf)_2$ + 5	2	163.74	47.6	
wt.% ANCl	5	133.33	46.9	
	10	97.66	46.0	
	1	130.16	47.5	16
	2	151.44	46.8	
$Zn(OTf)_2$ + Urea	3	132.12	41.1	
	4	195.79	38.6	
	5	164.09	39.0	
	1	192.06	42.8	26
2 M $ZnSO_4$ + 0.5	2	173.82	41.5	
M TAH	5	152.9	41.8	
	10	123.39	39.2	
	0.5	96.63	46.9	27
	1	90.03	46.4	
2 M $ZnCl_2$	2	86.27	46.8	
	5	79.67	46.6	
	10	69.5	.44.6	
1 m $Zn(ClO_4)_2$ +	0.5	222.65	53.0	This

				work
0.5 m NH_4Cl	1	199.56	51.7	
	2	184.21	50.3	
	4	150.6	49.9	
	6	117.4	48.9	
	10	81.25	48.9	

Table. S3. Kinetic parameters of CN7 electrolyte under different temperatures.

Temperature (℃)	**25**	**10**	**0**	**-20**	**25**
Warburg Coefficient (σ)	3.98	5.81	8.51	381.6	4.8
Diffusion coefficient (10^{-15} cm^2 s^{-1})	155.3	72. 7	33.9	0.02	106.6

Table. S4. Detailed comparison of low-temperature full-batteries performance with literature data.

Full battery (Anode//Cathode)	Electrolyte	Temperature (°C)	Time (day)	Capacity (mAh g^{-1})	Cycle number	Ref.
Li//LFP	HEPE	-20	248	80	500	28
Na//$Na_3V_2(PO_4)_3$@C	Composite materials	-20	125	68	500	29
Na//Ti_3C_2	/	-40	32	60	150	30
Na//AlF_3-$Na_{3.12}Fe_{2.44}(P_2O_7)_2$	/	-40	5	97	400	31
Zn//AC	$Zn(ClO_4)_2$	-30	280	50	7000	32
Zn//MnO_2	ZOTf-OQCNs	-30	90	150	5000	33
Zn//V_2O_5	$Zn(Otf)_2$	-20	167	170	2000	34
NCM811//Gr	APT	-20	125	124	100	35
Zn//PANI	$ZnSO_4$	-40	67	140	5000	36
$Zn_3(PO_4)_2$@Zn//KVOH ZnF_2	$Zn(Otf)_2$+TMP	-30	150	50	2300	37
Zn//V_2O_5	$Zn(CF_3SO_3)_2$	-40	21	41	2000	38
Zn//PANI@V_2O_5	P_5W_5	-20	250	82	1000	39
Zn//MnO_2/CNT	$ZnSO_4/H_2O$ DMSO	-20	50	176	300	40
Zn//Zn_2NC	$Zn(ClO_4)_2$	-20	73	120	7000	41
Zn//SnI_4	$Zn(ClO_4)_2$+NH_4Cl in PEG/H_2O	-20	493	180	9000	This work

References:

1. Hu, Y., et al. Novel insoluble organic cathodes for advanced organic K-ion batteries. *Adv. Funct. Mater.* **30**, 2000675 (2020).
2. Liu, M., et al. Amorphous organic-hybrid vanadium oxide for near-barrier-free ultrafast-charging aqueous zinc-ion battery. *Nat. Commun.* **15**, 10769 (2024).
3. Dai, Y., et al. Zn^{2+}-mediated catalysis for fast-charging aqueous Zn-ion batteries. *Nat. Catal.* **7**, 776-784 (2024).
4. Cao, Z., et al. Super-stretchable and high-energy micro-pseudocapacitors based on mxene embedded ag nanoparticles. *Adv. Mater.* **36**, e2401271 (2024).
5. Li, X., et al. Two-electron redox chemistry enabled high-performance iodide-ion conversion battery. *Angew. Chem. Int. Ed. Engl.* **61**, e202113576 (2022).
6. Wang, X., et al. Achieving a high-performance sodium-ion pouch cell by regulating intergrowth structures in a layered oxide cathode with anionic redox. *Nat. Energy* **9**, 184-196 (2024).
7. Lu, Y., Zhao, C.-Z., Huang, J.-Q., Zhang, Q. The timescale identification decoupling complicated kinetic processes in lithium batteries. *JOULE* **6**, 1172-1198 (2022).
8. Cao, W., et al. Tailoring C_3N_4 host to enable a high-loading iodine electrode for high energy and long cycling Zn-iodine battery. *ACS Energy Lett.* **10**, 320-329 (2024).
9. Bi, S., et al. Six-electron-redox iodine electrodes for high-energy aqueous batteries. *Angew Chem. Int. Ed. Engl.* **62**, e202312982 (2023).
10. Li, W., et al. Designing ternary hydrated eutectic electrolyte capable of four-electron conversion for advanced Zn-I_2 full batteries. *Energy Environ Sci* **16**, 4502-4510 (2023).
11. Han, W., Zhao, J., Li, X. Ternary chloride-free electrolyte design for highly efficient aqueous zinc-iodine batteries with four-electron conversion. *Inorganic Chemistry Frontiers* **11**, 5376-5383 (2024).
12. Wang, C., et al. Activating and stabilizing a reversible four electron redox reaction of I^-/I^+ for aqueous Zn-iodine battery. *Angew. Chem. Int. Ed.*, **136**:

e202403187 (2024).

13. Zhang, P. F., et al. Relocating conjugated 2p valence electrons in carbon host to stabilize I^+ for novel Zn-I_2 battery. *Adv. Energy Mater.* **15**, 2404845 (2025).
14. Yan, Y., Jiao, Y., Wu, P. Realizing high performance four-electron zinc-iodine batteries with acidic eutectic electrolyte. *Angew. Chem. Int. Ed.*, **64**, e202515633 (2025).
15. Qiu, C., et al. Unlocking high-performance four-electron zinc-iodine batteries through halogen bonding inversion and non-identical-frequency molecular vibrations. *Angew. Chem. Int. Ed.*, **137**: e202513747 (2025).
16. Li, C., et al. Urea chelation of I^+ for high-voltage aqueous zinc-iodine batteries. *ACS Nano* **19**, 2633-2640 (2025).
17. Zhu, F., et al. From inorganic to organic iodine: Stabilization of I^+ enabling high-energy lithium-iodine battery. *J. Am. Chem. Soc.*, **146**: 11193-11201 (2024).
18. Wu, H., et al. Quasi-solid cathode additive enables highly reversible four-electron $I^-/I^0/I^+$ conversion in aqueous Zn-I_2 batteries. *Adv. Mater.*, e11680 (2025).
19. Guo, J., et al. Aqueous zinc-organoiodine battery with high kinetics and dense cathodes. *J. Am. Chem. Soc.* **147**, 39652-39661 (2025).
20. Yi, Z., et al. Deciphering SN_2-type nucleophilic substitution via halogen-free intermediates for high-energy zinc-iodine batteries. *J. Am. Chem. Soc.* **147**, 26889-26897 (2025).
21. Liu, T., et al. Aqueous electrolyte with weak hydrogen bonds for four-electron zinc-iodine battery operates in a wide temperature range. *Adv. Mater.* **36**, e2405473 (2024).
22. Zong, W., et al. Dynamical Janus interface design for reversible and fast-charging zinc-iodine battery under extreme operating conditions. *J. Am. Chem. Soc.* **146**, 21377-21388 (2024).
23. Li, X., et al. Activating the I^0/I^+ redox couple in an aqueous I_2-Zn battery to achieve a high voltage plateau. *Energy Environ. Sci.* **14**, 407-413 (2021).

24. Li, X., et al. Anion-cation synergy enables reversible seven-electron redox chemistry for energetic aqueous zinc-iodine batteries. *Nano Energy* **138**, (2025).
25. Qiu C, Chen M, Pan Y, et al. Unlocking high-performance four-electron zinc-iodine batteries through halogen bonding inversion and non-identical-frequency molecular vibrations. *Angewandte Chemie* 137, e202513747 (2025).
26. Wang M, Meng Y, Sajid M, et al. Bidentate coordination structure facilitates high-voltage and high-utilization aqueous Zn-I_2 batteries. *Angewandte Chemie* 136, e202404784 (2024).
27. Kang J, Wang C, Liu Z, et al. Electron-outflowing heterostructure hosts for high-voltage aqueous zinc-iodine batteries. *Energy Storage Mater.* 68, 103367 (2024).
28. Guo, J., et al. Entropy-driven modulation of ion clustering and polymer crystallinity for low-temperature lithium metal batteries. *Angew. Chem. Int. Ed.* **64**, e202511612 (2025).
29. Yu, D., Zhang, W., Zhang, Q., Huang, S. Tuning anion chemistry enables high-voltage and stable potassium-based tellurium-graphite batteries. *Nano Energy* **92**, (2022).
30. Rui, X., et al. A low-temperature sodium-ion full battery: Superb kinetics and cycling stability. *Adv. Funct. Mater.* **31**, 2009458 (2021).
31. Ren, D., et al. Challenges and opportunities of practical sulfide-based all-solid-state batteries. *Etransportation* **18**, 100272 (2023).
32. Sun, Y., et al. Salty ice electrolyte with superior ionic conductivity towards low-temperature aqueous zinc ion hybrid capacitors. *Adv. Funct. Mater.* **31**, 2101277 (2021).
33. Zhu, Z., et al. Antifreeze protein mimics realizing stable low-temperature-resistant aqueous Zn-ion batteries with high water content. *Angew. Chem. Int. Ed.* **64**, e202505325 (2025).
34. Ma, Q., et al. Regulation of outer solvation shell toward superior low-temperature aqueous zinc-ion batteries. *Adv. Mater.* **34**, 2207344 (2022).

35. Kim, J. S., et al. Eutectic transition and interfacial modulation of multifunctional ionic liquid additives for subzero-temperature lithium-ion batteries. *Adv. Energy Mater.* **15**, e03900 (2025).

36. Wang, D., et al. Site-selective adsorption on ZnF_2/Ag coated Zn for advanced aqueous zinc-metal batteries at low temperature. *Nano Lett.* **22**, 1750-1758 (2022).

37. Wang, W., et al. Regulating interfacial reaction through electrolyte chemistry enables gradient interphase for low-temperature zinc metal batteries. *Nat. Commun.* **14**, 5443 (2023).

38. Wang, J., et al. Low-temperature and high-rate Zn metal batteries enabled by mitigating Zn^{2+} concentration polarization. *Chem. Eng. J.* **433**, 134589 (2022).

39. Wei, T., et al. Bonding interaction regulation in hydrogel electrolyte enable dendrite-free aqueous zinc-ion batteries from -20 to 60 ℃. *Chem. Eng. J.* **434**, 134646 (2022).

40. Feng, D., et al. Immunizing aqueous Zn batteries against dendrite formation and side reactions at various temperatures *via* electrolyte additives. *Small* **17**, 2103195 (2021).

41. Dong, C., et al. Tailoring zinc diatomic bidirectional catalysts achieving orbital coupling-hybridization for ultralong-cycling zinc-iodine batteries. *Energy Environ. Sci.* **18**, 3014-3025 (2025).